INT. J. REMOTE SENSING, 2003, VOL. 24, NO. 7, 1469–1486

Virtual surfaces simulating the bidirectional reflectance of semiarid soils

J. CIERNIEWSKI† and A. KARNIELI‡

†Department of Physical Geography and Remote Sensing, Institute of Physical Geography, Adam Mickiewicz University in Poznan, Poland;
e-mail: ciernje@main.amu.edu.pl
‡The Remote Sensing Laboratory, Jacob Blaustein Institute for Desert Research, Ben Gurion University of the Negev, Israel

(*Received 10 November 1999; in final form 23 July 2001*)

Abstract. Virtual surfaces of four semiarid soils—regs, crusts, playas and sands—used to predict their bidirectional reflectance in the optical domain are discussed in the paper, on the background of their real equivalents and their directional reflectance characteristics. These surfaces are defined by the horizontal and vertical semiaxes of equal-sized opaque spheroids simulating their particles or aggregates. The spheroids are regularly dispersed into a net of squares of a given side length on a freely sloping plane. They are absorbed into the ground with their tops projecting to a given height above the slope. The material of the vertical structure is additionally defined by its refractive index. Virtual surfaces determined in this way were used as part of the input data to a geometrical model, which predicts the soil surface normalized reflectance (*NR*), expressed as the ratio of the total radiance of the simulated surface viewed from the off-nadir direction to the radiance viewed from the nadir.

1. Introduction

Information about interpreted objects recorded in remote sensing images in the optical domain is transmitted by electromagnetic radiation reflected from the surface of the objects. Bare soils, like many natural objects, show variation in their radiance due to the direction of irradiating solar energy and the direction along which the reflected energy is viewed by ground-based, airborne and satellite sensors. Soil surface irregularities—caused by the soil texture, aggregates and micro-relief configuration, which are large compared with the wavelengths, and that are opaque—cast shadows on the surfaces. The variation caused by the shadows when viewed by the sensors is the basic reason for the soil bidirectional reflectance behaviour, because the wave energy leaving the shaded areas is many orders of magnitude smaller than the energy reflected from the sunlit soil fragments.

Cultivated soils with dominant diffuse features usually seem to be brightest when sensed from the direction that gives the lowest proportion of shaded fragments. Those soil surfaces usually display a clear backscattering character with a reflectance peak towards the Sun position and decreasing reflectance in the direction away from the peak. Laboratory results presented by Coulson (1966) show that desert soil

International Journal of Remote Sensing
ISSN 0143-1161 print/ISSN 1366-5901 online © 2003 Taylor & Francis Ltd
http://www.tandf.co.uk/journals
DOI: 10.1080/01431160110119425

materials like gypsum sand and beach quartz sand display a high reflectance and a strong forwardscatter maximum for wavelengths in the visible and near-infrared range. The directional reflectance of these soil surfaces clearly varies with the angle of the incident radiation. The backscatter, as well as the forwardscatter, regimes in soil reflectance in the optical domain have been identified by Deering *et al.* (1990). They have been demonstrated with examples from an alkali flat bare soil and dune sand surface. The first surface, which comprised a coarse texture and bright-stabilized crust with intermittent darker patches, displayed the distribution pattern of strong backscatter reflectance. The second surface, composed of nearly pure gypsum crystals creating uniform wind ripples, showed forwardscatter as its predominant feature. The sharp peak in the forward direction manifests a considerable contribution of the specular component to total reflectance from these fine gypsum sand grains, derived from selenite flakes. Shoshany (1993), collecting more than 70 data sets for different types of desert stone pavements and rocky surfaces in Australia under varied illumination conditions, found that most of the surfaces exhibited an anisotropic reflection with a clear backscattering component. Eaton and Dirmhin (1979) observed that predominant forwardscatter also characterized natural surfaces like snow and salt flats. Most geometrical soil directional reflectance models that have been proposed predict soil reflectance based on the assumption that shadowing from soil irregularities has a greater influence than the scattering properties of a soil material at the micro-scale. Walthall *et al.* (1985) express bidirectional reflectance of a bare soil surface as a three parameter function of view direction to the solar direction. These parameters of an empirical character are not explicitly related to soil surface properties. The function cannot be used to predict soil reflectance distribution for soil surfaces other than those analysed. Soil aggregates in the model of Norman *et al.* (1985) were simulated with cuboids. The bidirectional reflectance distribution function for the simulated soil surface shows a clear backscatter regime. The height of soil surfaces in the Monte Carlo reflectance model of Cooper and Smith (1985) varied periodically with the cosine function in one of two directions. It assumes that the soil is a perfectly diffuse reflector at the microscopic level, such that the probability that a photon will be scattered at a given angle only depends on the orientation of the soil surface irregularities. The diffuse character of the model also shows a backscattering regime of the soil directional reflectance. Hapke's models (1981, 1984, 1986), developed for the interpretation of reflectance properties of planetary surfaces, produce bidirectional signatures like those of a medium composed of particles characterized by a single-scattering albedo and a phase function. The models take into account a parameter that depends upon regolith porosity and particle size distribution. The models, as used by Pinty *et al.* (1989), have five input parameters: a single scattering coefficient, two parameters describing the hot spot phenomenon, and two parameters describing the scattering phase function. Jacquemoud *et al.* (1992) added to Hapke's model a specular contribution and separated those parameters that depend on wavelength from those that are not wavelength-dependent. The model of Irons *et al.* (1992) describes a soil surface consisting of uniform opaque spheres regularly spaced on a horizontal surface. The geometry of the structure is defined as the area of a single sphere in its horizontal projection in a circle of unit area of the horizontal surface. Both direct and isotropically diffuse light illuminate the soil surface. The spheres and background are Lambertian. Soil reflectance is expressed as a function of the horizontal area shaded by the spheres, the sunlit fraction and the proportion of diffuse illumination.

Otterman's model (Otterman 1981, Otterman and Tucker 1985, Deering *et al.* 1990) treats bare soils as composed of thin vertical cylinders of variable heights with facet-reflectance and transmittance located randomly on an horizontal plane with Lambertian reflectance. The architecture of the soil protrusions is described by a parameter that is the sum of the height times the diameter of these cylinders per unit horizontal area. The model assumes that the facet-reflectance largely controls the backscatter while facet transmittance is responsible for determining forwardscattering. This was the first model simulating both backscattering and forwardscattering. It predicted a clear forwardscattering character of reflectance for a surface with nearly pure gypsum crystals of high transmittance. The models of Cierniewski (1987, 1989) desribes soil aggregates as regularly spaced equal-sized opaque spheres, while Cierniewski and Verbrugghe's models (1994) simulate them by spheroids of a defined proportion of their vertical to horizontal radii. All the models assume only perfectly diffuse reflection from the sunlit soil fragments. Improved versions of the models, describing bidirectional reflectance from non-directional rough soil surface with regular dispersed soil aggregates, also take into account specular features of the soil material (Cierniewski *et al.* 1996, Cierniewski and Verbrugghe 1997). The models assume that the energy leaving a given sunlit facet of the geometrical structures has a specular-diffuse character. A part of the direct energy is reflected as from a near-perfectly-specular object and the other part as from a perfectly diffuse one. The first model describes the distribution of the energy leaving soil surfaces by the empirical function, while the second one uses the Fresnel equations treating reflected light as unpolarized. The reflectance of the simulated soil surface is finally expressed by the normalized reflectance factor, defined as the proportion of the total radiance measured from the off-nadir direction to the radiance measured from the nadir.

A new model, developed by Cierniewski (1999), simulates soil particles or aggregates as opaque spheroids. They are spatially regularly dispersed and partially buried in the ground of the plane on which they are distributed. The simulated surface is illuminated by the direct solar beam as well as diffuse light. The model assumes that the electromagnetic energy leaves the surface in both the diffuse and the specular ways.

The aim of this paper is to apply the above model to four arid soil surfaces that differ by texture and roughness. Their virtual surfaces were used for predicting the soil bidirectional reflectance.

2. Methodology

2.1. *The study area*

This research was conducted in a sand dune environment located in the north-western Negev desert (Israel) near the border between Israel and Egypt. The region is semiarid with 100 mm of mean annual rainfall, concentrated during the winter months (October to April). The area is characterized by sparse higher vegetation cover. The perennials cover about 14% of the area; annuals vary from null during the dry seasons to about 27% in the spring when they exhibit peak biomass. Consequentially, from the remote sensing point of few, it is quite obvious that the soil background is the dominant feature that contributes to the overall spectral response of the region.

Due to limited human and animal activities in the Negev, most of the region consists of stabilized linear dunes (Karnieli and Tsoar 1995). Four morphological units of various texture compositions as well as differet surface roughnesses exist in the study area: regs, crusts, playas and sands. These units were selected to be the objects of our research:

1. *Regs* (figure 1a): at the edges of the dune area there are isolated patches, a few hundred square metres in area, of reg soils, which are also denoted as desert pavement. Gravel and flint fragments (a few centimetres in diameter) that are a product of *in situ* weathering cover these surfaces. The patches contain very little soil (mostly fines), which occurs in the interstices between the stones of the pavement, thus the stones are partially submerged beneath the surface and partially above (Evenari *et al.* 1982).
2. *Crusts* (figure 1b): the basal dune and interdune corridors extend over some 85% of the area. The surface is covered by a rather contiguous biogenic soil crust consisting mainly of cyanobacteria where *Microcoleus vaginatus* is the dominant species accompanied by *Scytonema*, *Schizothrix*, *Calothrix*, *Chroococcidiopsis*, *Nostoc* and *Phormidium* (Danin *et al.* 1989, Danin 1991, Karnieli 1997). During the dry periods, the cyanobacteria is located just beneath the soil surface. This crust of a few millimetres depth glues the soil particles together, mainly fines (silt and clay, up to about 40%) and has a relatively high organic matter content (1–2%). Therefore, biological soil crusts play a major role in dune stabilization. The micro relief of the biogenic soil crusts is relatively rough and characterized by many small depressions.
3. *Playas* (figure 1c): also in the interdune corridors exist the playa surfaces, which are flat whitish isolated patches of up to a few hundred square metres in area. These playas are relics of an old flood plain, consisting of up to 70% fines and almost not containing any microphytic communities. Therefore, the playa crusts are considered as a physical crust. When dry, they form polygons

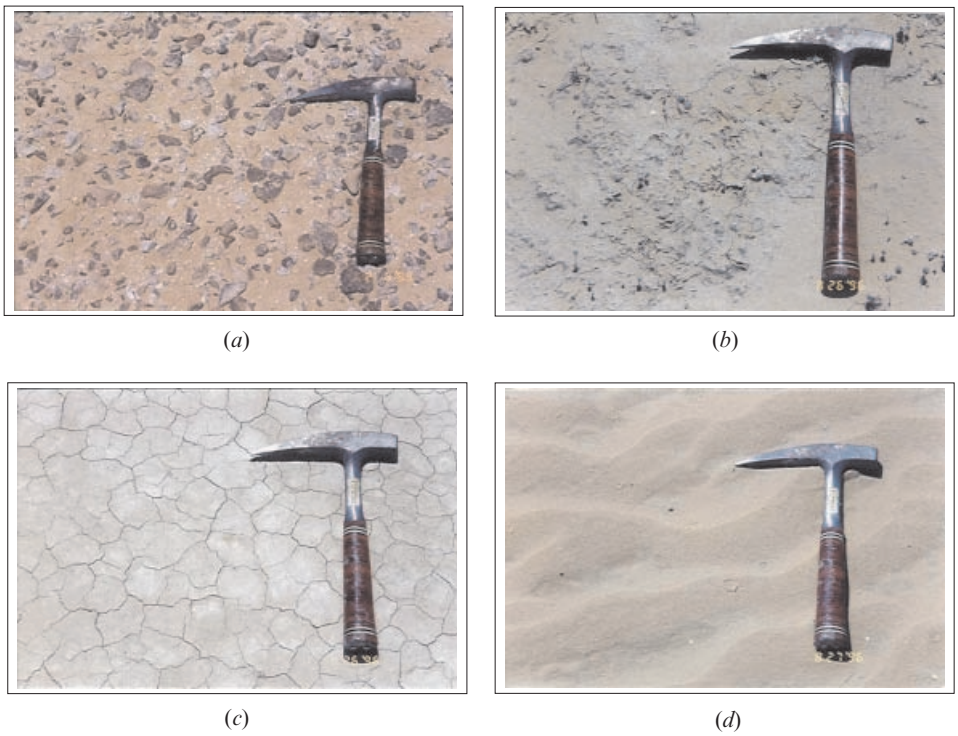

(*a*) (*b*)

(*c*) (*d*)

Figure 1. Close-up view of the soil surfaces: (*a*) reg, (*b*) crust, (*c*) playa and (*d*) sand.

of cracks of different shapes, each of a few hundred square centimetres. The playa surface is very smooth.

4. *Sands* (figure 1d): the dune crests sited at the upper part of the sand ridge cover some 10% of the area. They are composed of about 98% unconsolidated active sand. The organic matter content is very low (0.1%). Although the surface is relatively smooth, the wind causes uniform ripple features on top of the sand formation.

2.2. *Measurements*

Four data sets were acquired for each ground unit in August 1996 and June 1999 during several days of measurements. Ground radiometric measurement was done with a CIMEL 313-21 radiometer at 10°-sensor field of view (FOV). This instrument measures luminance in four different wavelengths: 550, 650, 850 and 1650 nm. The sensor was held at 2.5 metres above the surface by attaching it to a BRDF apparatus, resulting in a 43.7 cm diameter sample view area, at nadir. The apparatus was rotated according to the solar principal plane. Each sequence, lasting about 6 min, contains measurements from $-70°$ (forward, toward the Sun) to $+70°$ (backward, away from the Sun) in 10° increments. Nadir measurements were conducted at the beginning and at the end of each sequence (total of 17 measurements in each sequence). The apparatus was moved from one unit to another during the day, from sunrise to sunset, thus we obtained between 5 and 11 sequences of data for each unit.

Ground roughness was measured with a special device called BGUGSS 1800, invented by the Geography Department of Ben Gurion University of the Negev. This laser-based equipment, mounted on a tripod about 1.8 m above the ground, measures the surface roughness in an area of 87×87 cm of the ground beneath. The vertical accuracy of this instrument is 1.5 mm and the spatial resolution is 1 cm.

The roughness state of these surfaces was quantitatively assessed with a roughness index (RI), which expresses the average height deviation between each pixel x_i of a given surface and the eight closest pixels surrounding it x_s, averaged for the entire measured area with the following equation:

$$RI = \frac{\sum_{i=1}^{m_p} \left(\sum_{j=1}^{n_p} |x_i - (x_s)_j| \right) \Big/ (n_p)}{m_p - 4(\sqrt{m_p} - 1)} \tag{1}$$

where n_p and m_p denote the number of pixels in each moving window and the total number of pixels of given surface which are 8 and $87^2 = 7569$, respectively.

2.3. *The model*

The virtual soil surfaces were originally used as part of the input data for modelling the distribution of electromagnetic radiation in the optical domain reflected from a rough soil surface. The roughness is caused by irregularities of soil particles or aggregates dispersed regularly in all directions.

Equal-sized opaque spheroids of horizontal, a, and vertical, b, radii lying on a plane sloping at angle ε, simulate the soil surface (figure 2). They are absorbed into the ground of the slope plane, with their tops projecting at height t above the ground. These spheroids are regularly arranged on the slope plane such that their centres are in a square grid of interval d. The resulting geometrical surface structure is illuminated by direct solar beams at zenith angle θ_s as well as diffuse light. A sensor

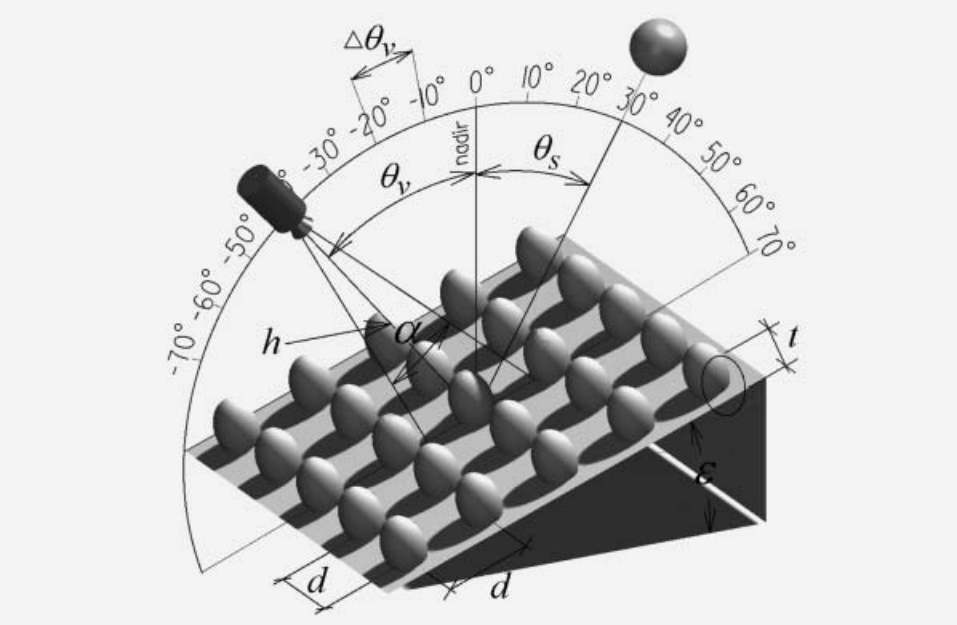

Figure 2. Schematic representation of the model geometry.

is suspended over the simulated soil surface for observing it along the solar principal plane *SPP* at zenith angles θ_v, with $\Delta\theta_v$ increments in the forwardscattering and backscattering directions, represented by negative and positive values of the θ_v, respectively. The sensor defines the angle α with its field-of-view and is located at a distance of h away from the observed point.

In the first step of the calculation for a given profile, the position of all the border points between the directly illuminated and shaded fragments of the geometrical structure is computed. The amount of the radiative energy coming directly to the illuminated individual facet *fa* of the geometrical structure, the ellipse and the soil slope between the ellipses, defines the factor $Ei^{\downarrow}_{v\,fa}$:

$$Ei^{\downarrow}_{v\,fa} = \cos\theta_s\cos\beta + \sin\beta + \sin\theta_s\cos(\phi_r - \phi_s) \tag{2}$$

where β is the slope angle of the facet, and ϕ_r and ϕ_s are the azimuth angles describing the positions of the facet and the Sun, respectively. The value of this factor, $Ei^{\downarrow}_{v\,fa}$, equals the cosine of the incidence angle γ of the direct solar beams to the facet, measured with respect to its normal. It expresses the vector length of the energy leaving the facet along the normal. The energy leaving the directly illuminated facets $Ei^{\downarrow}_{v\,fa}$ is directly proportional to the energy incident on it $Ei^{\downarrow}_{v\,fa}$. The $Ei^{\uparrow}_{v\,fa}$ is in part perfectly diffused, and in part reflected in a specular way. The model assumes that the length of the reflected energy vector in a given direction θ_v is the sum of the lengths of these two vectors (i.e. the perfectly diffused energy $Edi^{\uparrow}_{(\theta v)\,fa}$ and the energy specularly reflected $Esp^{\uparrow}_{\theta v\,fa}$ (figure 3)):

$$Ei^{\uparrow}_{\theta v\,fa} = Edi^{\uparrow}_{\theta v\,fa} + Esp^{\uparrow}_{\theta v\,fa} \tag{3}$$

The length of the vector $Esp^{\uparrow}_{\theta v\,fa}$, describing unpolarized light, depends on the

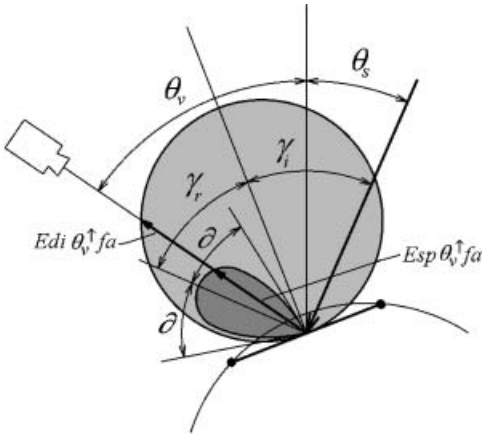

Figure 3. Distribution of the energy leaving a facet of a simulated soil surface in the specular and diffuse modes.

polarization $Fp_{(\gamma)}$ of the reflected light $Ei^{\downarrow}_{v\,fa}$ at angle γ_i, as follows:

$$Esp^{\uparrow}_{\theta v\,fa} = Ei^{\uparrow}_{v\,fa} Fp_{(\gamma i)};\ Fp_{(\gamma_i)} = \frac{r_{\perp}^2 + r_{=}^2}{2} \tag{4}$$

where $r_{\perp}$ and $r_{=}$ are respectively the perpendicular and parallel Fresnel reflection coefficients, given by:

$$r_{\perp} = \frac{-n^2\cos\gamma_i + \sqrt{n^2 - \sin^2\gamma_i}}{n^2\cos\gamma_i + \sqrt{n^2 - \sin^2\gamma_i}};\ r_{=} = \frac{\cos\gamma_i - \sqrt{n^2 - \sin^2\gamma_i}}{\cos\gamma_i + \sqrt{n^2 - \sin^2\gamma_i}}$$

where n is the refractive index of the soil surface. The vector of the energy specularly reflected is oriented in such a way that the angle of incidence, γ_i, equals the angle of reflection, γ_r. As the vector of the quasi-specular reflected energy, it is visible inside the limited angle range defined by the angle $2\ \partial$ around the direction of reflection $\gamma_r \pm \partial$, where $\gamma_r = \theta_s - 2\gamma_i$. The model assumes that the length of the vector $Esp^{\uparrow}_{\theta v\,fa}$ decreases to zero linearly from this direction γ_r to the range limit.

The length of the vector $Ei^{\uparrow}_{\theta v\,fa}$ completes the diffuse component $Edi^{\uparrow}_{\theta v\,fa}$ defined as:

$$Edi^{\uparrow}_{\theta v\,fa} = (1 - Fp_{(\gamma_i)}) Ei^{\uparrow}_{v\,fa} \cos\theta_v. \tag{5}$$

Finally, the total energy $Eis^{\uparrow}_{\theta v\,fa}$, leaving a given directly illuminated facet fa and reaching the sensor oriented at an angle θ_v, is sensed as the amount $Ei^{\uparrow}_{\theta v\,fa}$ divided by the cosine θ_v.

The diffuse light $Esk^{\downarrow}_{fa}$ reaches the soil surface fragments directly illuminated by the sun beams, as well as the shaded fragments. Its amount is limited by the presence of adjoining spheroids (ellipses in profiles), which reduce the amount of diffuse energy relative to the condition when it comes from the complete hemisphere. As a result, the additional portion of the energy dispersed from a given facet is described as follows (figure 4):

$$Esk^{\uparrow}_{fa} = f_{di}\frac{\delta}{180^{\circ}} \tag{6}$$

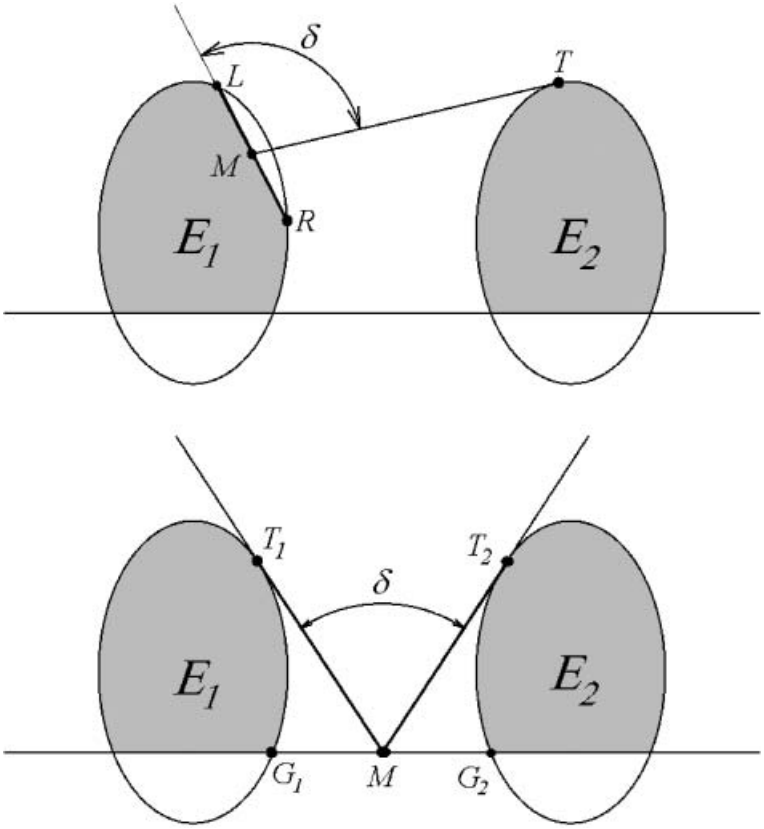

Figure 4. Limitations in illumination by skylight of the facet segment LR on the ellipse E_1 and the slope plane between ellipses E_1 and E_2, expressed by the angle δ. M is the middle point of the segments LR and G_1G_2. T, T_1 and T_2 are the tangent points from the sides to the neighbouring ellipses forming the angle δ.

where f_{di} approximates a reflectance effect from soil surfaces illuminated only by the diffuse light component and is defined as part of the direct solar beam's energy.

The radiance factor of the simulated soil surface, with directly illuminated and shaded fragments, viewed by the sensor from a given direction θ_v along a given profile pr, is defined as:

$$L^{\uparrow}_{\theta v\, pr} = \sum_{i=1}^{j}\left[\left(Eis^{\uparrow}_{\theta v\, fa_{(i)}} + Esk^{\uparrow}_{fa_{(i)}}\right)\xi i_{fa_{(i)}}\right] + \sum_{i=1}^{j}\left(Esk^{\uparrow}_{fa_{(i)}}\xi s_{fa_{(i)}}\right) \tag{7}$$

where i is the i^{th} facet of the geometrical structure, $\xi i_{fa_{(i)}}$ and $\xi s_{fa_{(i)}}$ are the elementary view angles of the illuminated and the shaded i^{th} facet, respectively. The radiance of the simulated soil surface reaching the sensor through its field-of-view $L^{\uparrow}_{\theta v\,\text{FOV}}$ is the sum of the values calculated along the individual profiles $L^{\uparrow}_{\theta v\, pr}$ and the space between the spheroids.

Finally, the reflectance from a rough soil surface along the solar principal plance SPP is described by the normalized reflectance $NR_{(\theta v = SPP,\, \theta v)}$, which is defined as the ratio of the total radiance $L^{\uparrow}_{\theta v\,\text{FOV}}$ measured from the off-nadir direction θ_v to the radiance measured from the nadir. Assuming that the normalized surface reflectance

$NR_{(\theta v = SPP, \theta v)}$ in the plane OP perpendicularly oriented to the SPP for each of the view zenith angles θ_v is 1 and the ratio in the function of the ϕ_v between the SPP and the OP has a simple linear distribution, its value $NR_{(\phi v, \theta v)}$ for any observation plane can be defined as:

$$NR_{(\phi_v, \theta_v)} = NR_{(\phi_v = SPP, \theta_v)}\left(1 - \frac{\phi_v}{90^\circ}\right) + \frac{\phi_v}{90^\circ} \tag{8}$$

where ϕ_v is the relative horizontal angle of the observation plane measured from the SPP. The model is applicable, when the observation plane goes along the direction of the highest sloping line of a simulated surface. The model, presented above was prepared in the form of a computer program, written in Pascal.

2.4. *Fitting of the virtual surface geometry*

The geometry of the virtual surfaces discussed in the paper was obtained by the inversion of the model described in this work. The fitting of the geometrical parameters to the soil reflectance measurements involves choosing those values of the input parameters, which give us the lowest possible root mean square error (*rms*) between the modelling and the measured distribution of the normalized surface reflectance (*NR*) as a function of view zenith angle. *These* parameters include the spheroid vertical radius b, the distances between the spheroids d, the height of spheroid tops above the ground t, completed by the refractive index of the soil surface n, and the ratio of the reflected diffuse light f_{di} for a given wavelength. The horizontal radius of the spheroids a, was evaluated as its average value for a given surface. Other parameters describing conditions of illumination and observation of the studied soil surfaces, θ_s, h, α, were taken as their measured values.

This fitting was performed automatically using a special computer procedure. A program, written in Object Pascal, automatically fits the geometrical parameters of the analysed soil surfaces. It is realized in two stages. In the first one, for a surface at each solar zenith angle θ_s, the program computes the $rms_{\theta_s, s}$ using the following formula:

$$rms_{\theta_s, s} = \frac{1}{nv - 1}\sqrt{\sum_{nv-1}^{nv}\left(M_{\theta_s, \theta_v} - P_{\theta_s, \theta_v, s}\right)^2} \tag{9}$$

where nv is the number of θ_v, M_{θ_s, θ_v} is a measured value of the NR for given angles θ_s and θ_v, $P_{\theta_s, \theta_v, s}$ is a predicted value of NR for these two angles and the set s of parameters: b, t, d, n and f_{di}. All data collected when the luminancemeter cast a shadow on the observed surface were eliminated from the calculation. In the second stage, the program determines the quantities K_s:

$$K_s = \sum rms_{\theta_s, s} \tag{10}$$

where the sum is spread over all values of θ_s. Finally, the minimum value along the computed K_s's is found and it indicates the set s for which the average root mean square is the lowest.

3. Results and discussion

3.1. *Roughness of soil surfaces*

The roughness of the four soil surfaces analysed in this paper are illustrated in figures 5a–d. The lowest roughness corresponds to the playa surface (figure 5c), whose height variation does not exceed 10 mm. The height irregularities are a

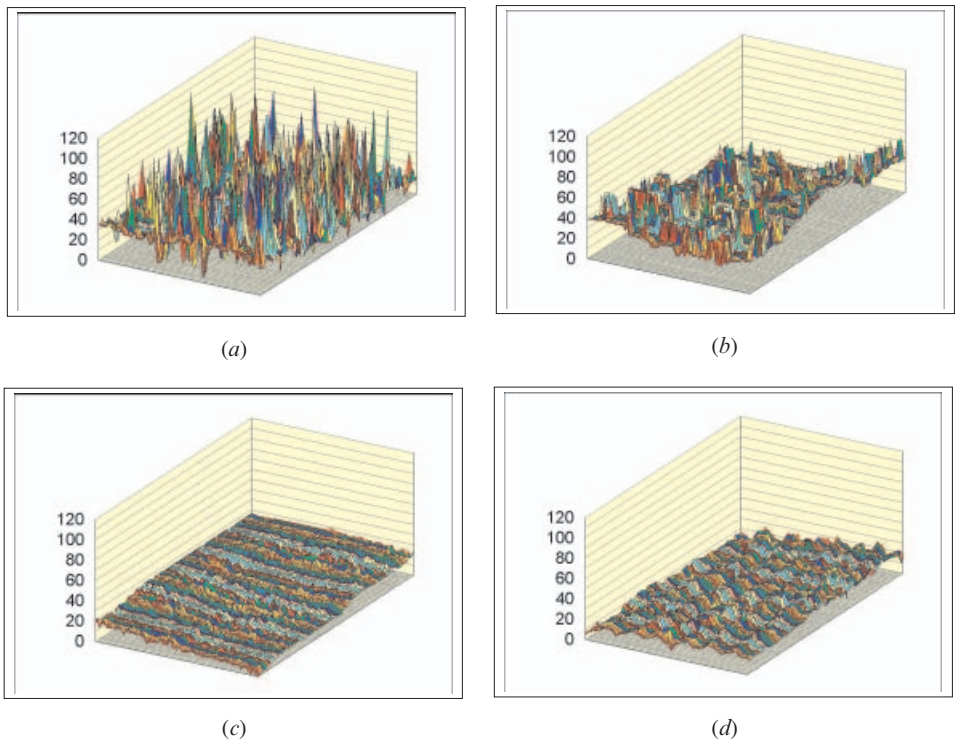

Figure 5. Soil surface roughness as obtained from the BGUGSS equipment data: (*a*) reg, (*b*) crust, (*c*) playa and (*d*) sand.

consequence of cracks on the surface between the physical crust polygons. Similarly, the dune sand surface shows low roughness characteristics (figure 5d). Its maximum height variation reaching 15 mm is the effect of ripplemarks. The biological crust (figure 5b) creates a clearly irregular plane with maximum irregularities of about 20 mm that are randomly spread over the surface. The highest roughness is exhibited by the reg surface (figure 5a). Flint fragments lying on this surface generate irregularities often exceeding 70 mm in height. Roughness index (RI) (equation (1)) values of 1.22 mm, 1.53 mm, 3.24 mm and 7.39 mm were obtained for the playa, sand, crust and reg surfaces, respectively.

3.2. *Virtual soil surfaces*

The following assumptions were made while fitting the parameters of these virtual surfaces:

1. All the parameters describing the geometry of a studied surface (a, b, t and d) at a given roughness state are independent of the illumination and viewing conditions; their values were fitted with a precision of 0.005 cm, except those describing the reg surface, which were fitted with the precision of 0.1 cm.
2. For a given wavelength the refractive index n of a soil surface, as well as the reflected diffuse light f_{di}, is independent of the solar zenith angle θ_s; their values were fitted with a precision of 0.05.

All the model-generated data were obtained with the ratio of the diffuse light of 0.05

independent of wavelength, assuming that a higher proportion of the diffuse light in the energy illuminating the target at lower wavelengths is compensated by its corresponding higher absorption at lower wavelengths after reflection. It was also assumed that the vectors of the quasi-specular component of the reflected energy were visible around the direction of reflection whose angular distance ∂ equals 30°. This was practically fixed as the best value for the normalized reflectance curves for all the analysed soil materials (figure 6). The model executed the calculation of the soil directional reflectance along the five 2-D profiles, dividing into three segments each curve-linear fragment of a soil geometrical structure viewed by the sensor as an individual category of the directly illuminated and shaded soil surface.

The values of all of these virtual surface parameters fitted by the inversion of the model are listed in table 1 and presented in figures 7a–d. The sizes of these virtual surfaces have been linearly enlarged with respect to their real equivalents on the ground. The enlargement factors are 0.25×0.25 cm for the playa and the sand, 2.5 cm × 2.5 cm for the crust, and 25×25 cm for the reg. All the surfaces are presented in the same illumination and viewing conditions.

The virtual reg surface (figure 7a) is essentially different in terms of its size, its irregularities and its shape compared to the other analysed surfaces. It is described by the spheroids with the highest vertical elongation ($b/a = 4$). The virtual surface simulating the crust (figure 7b), like in nature, is rough as well. It is described by the spheroids touching each other with a vertical elongation b/a of 1.2 and a relatively small absorption into the plane of the ground, which is the lowest in relation to the other analysed surfaces ($t/a = 1$). The playa material (figure 7c), essentially smoother and characterized by a finer texture, is simulated by spheroids 2.5 times lower in height than their horizontal radius a in relation to the spheroids of the remaining surfaces. The virtual playa's spheroids are the most flattened ($b/a = 0.8$). They are absorbed deepest into the ground and arranged with larger distances between them than the crust's spheroids. Probably, the cracks on the dried playa material prevent its virtual surface from being the smoothest among the analysed surfaces, even though its texture may indicate so. The sand surface (figure 7d) represents the smoothest virtual surface. Although it is described by less vertically elongated spheroids ($b/a = 1.1$), these are the deepest absorbed into the ground ($t/a = 0.7$) and have the highest proportion of flat spaces between their emerged fragments compared to the other surfaces.

One geometrical parameter of these virtual surfaces corresponds to real shape of the studied surfaces. It is the horizontal radius of the spheroids a, which in accordance with the assumption of the virtual surfaces fitting equals in approximation the average radius of irregularities of these surfaces. It causes that general shape of these studied surfaces and their virtual equivalents is rather similar. In this initial stage of the studies, a quantitative relation between the roughness state of the real surfaces, described by their RI, and a similar roughness parameter of the virtual surfaces was not found.

3.3. *The normalized reflectance curves*

The high proportion of flat spaces between the spheroids and the spheroids themselves (with almost spherical cross sections and relatively flat tops) for the sand virtual surface produced the lowest variation of its NR in the entire range of the view zenith angle function along the solar principal plane SPP for solar zenith angles θ_s lower than 40° (figure 6). For θ_s higher than 40°, its NR variation clearly grows in the forwardscattering directions as a consequence of its specular effects, the most intensive along the four analysed soil surface types. The flatness of the playa's virtual surface spheroids

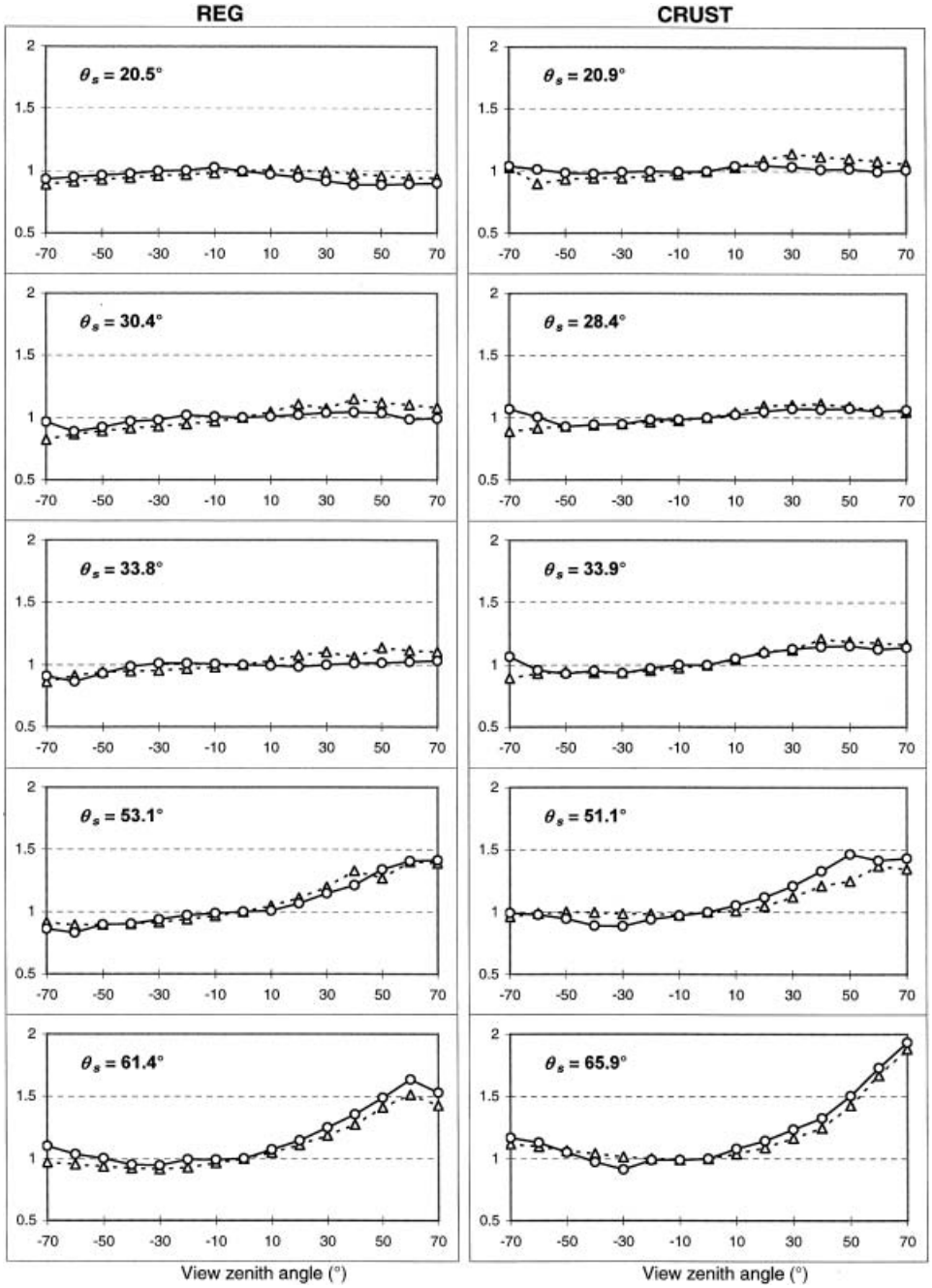

Figure 6. Relation between the normalized reflectance (NR) of the analysed soil surfaces along the solar principal plane for the 850 nm channel predicted by the model (solid line) and measured (dashed line) for selected solar zenith angles θ_s.

has caused its NR curves to resemble those of the sand surface more than those of the crust. The virtual surface representing the crust, whose high roughness is caused mainly by the small absorption of the virtually elongated spheroids into the ground, yielded

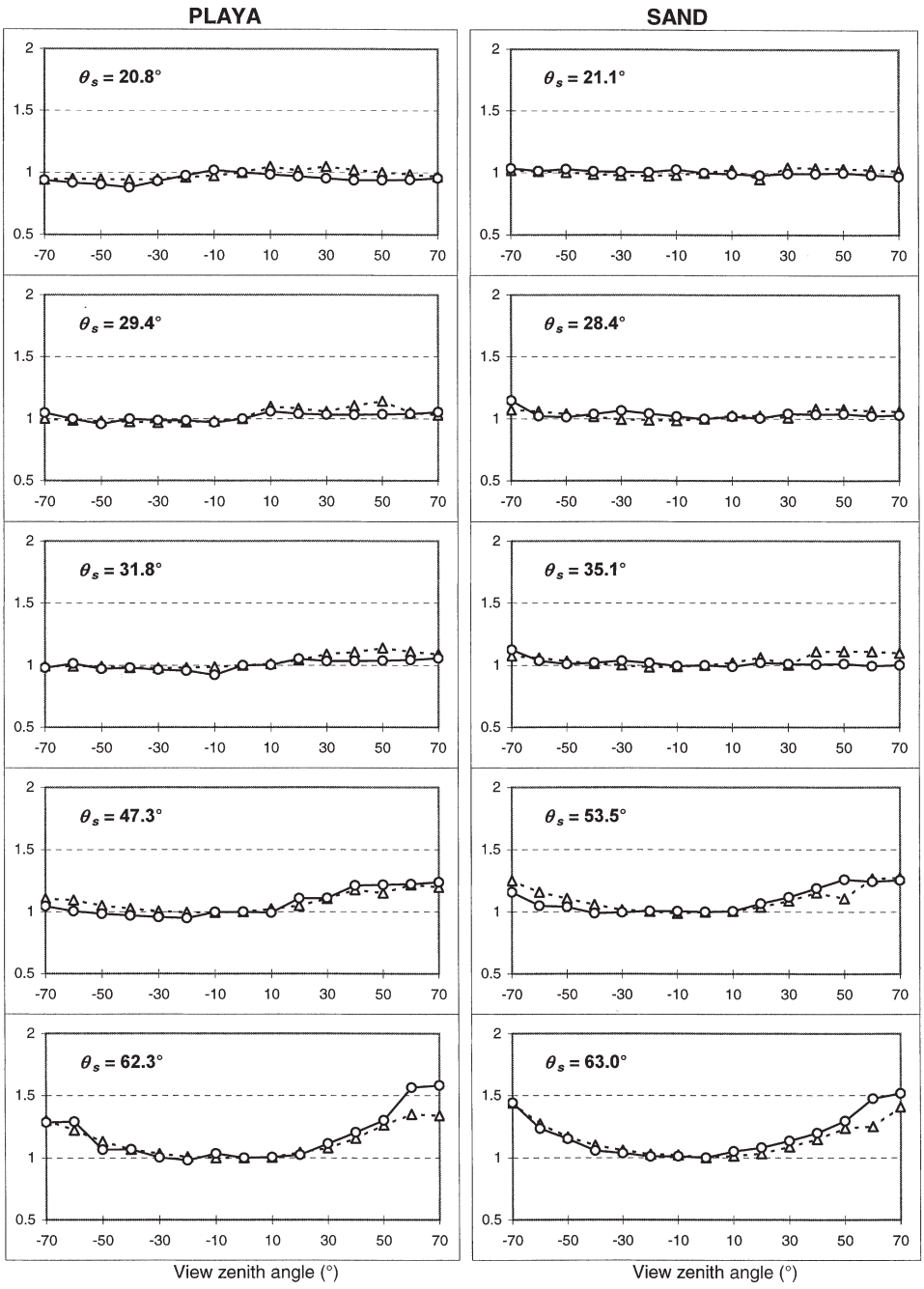

Figure 6. (*Contd*).

NR curves with essentially less visible specular effects in the forward scattering range. However, this curve shows the highest variation of the normalized reflectance in the backscattering range. The shapes of the *NR* curves for the crust are very similar to those of the reg, especially in the backscattering range. The reg *NR* curves demonstrate specular effects weakly in the forwardscattering range.

Table 1. Geometry and the refractive index n of the virtual surfaces.

					n			
Surface	a (cm)	b/a	t/a	d/a	550 nm	650 nm	850 nm	1650 nm
Reg	1.000	4.0	0.7	1.75	2.6	2.5	2.3	2.3
Crust	0.250	1.2	1.0	2.00	2.9	2.5	2.3	2.3
Playa	0.010	0.8	0.9	2.15	2.1	2.0	1.9	1.9
Sand	0.025	1.1	0.7	2.00	2.2	2.0	1.9	1.8

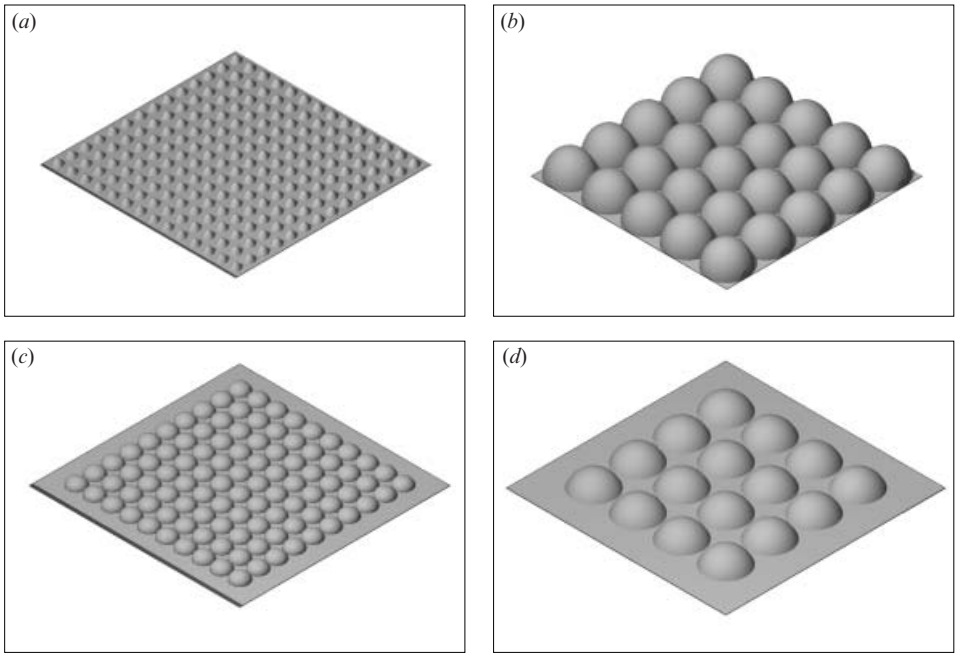

Figure 7. The virtual equivalents of the soil surfaces: (*a*) reg 25×25 cm; (*b*) crust 2.5×2.5 cm; (*c*) playa 0.25×0.25 cm; and (*d*) sand 0.25×0.25 cm.

Measured and model-generated NR curves related to the near-infrared channel (850 nm) in figure 6 show good mutual fitting. The goodness of fit depends on wavelength (table 2). For all the analysed soil surfaces, the fitting accuracy for the green light (550 nm) is the lowest. It is clearly higher for the red light (650 nm) and highest for the near-infrared (850 nm), as well as for the middle-infrared (1650 nm).

3.4. *Spectral contrast between the analysed surfaces*

The high fitting accuracy between the measured and the model generated data enables us to predict the reflectance behaviour of the analysed soil surfaces under any illumination and observation conditions using their virtual surfaces. Figure 8 shows the distribution of the reflectance (R) of these soil surfaces at 850 nm as a function of the view zenith angle for some chosen solar zenith angles along the solar principal plane, where R variation is the highest. Use of the R, which expresses the proportion of soil radiance to the radiance of a standard reflectivity panel, also

Table 2. Root mean square error (*rms*) for measured and predicted reflectance data generated by the model using the virtual surface parameters.

		rms			
Surace	θ_s	550 nm	650 nm	850 nm	1650 nm
Crust	20.9	0.030	0.023	0.018	0.015
	28.4	0.022	0.019	0.016	0.016
	33.9	0.025	0.018	0.015	0.015
	51.1	0.013	0.016	0.020	0.024
	65.9	0.018	0.024	0.016	0.021
	Average	0.022	0.022	0.017	0.018
Playa	20.8	0.022	0.017	0.015	0.014
	29.4	0.016	0.010	0.012	0.008
	31.9	0.022	0.015	0.012	0.012
	47.3	0.017	0.010	0.014	0.017
	62.3	0.014	0.017	0.014	0.020
	Average	0.018	0.014	0.013	0.014
Sand	21.1	0.025	0.017	0.010	0.010
	28.4	0.025	0.017	0.012	0.012
	35.1	0.035	0.021	0.018	0.012
	53.5	0.025	0.018	0.014	0.017
	63.0	0.012	0.010	0.013	0.020
	Average	0.024	0.017	0.013	0.014
Reg	20.5	0.028	0.027	0.021	0.022
	30.4	0.038	0.034	0.028	0.025
	33.8	0.029	0.024	0.019	0.015
	53.1	0.024	0.018	0.013	0.016
	61.4	0.019	0.025	0.020	0.024
	Average	0.028	0.026	0.020	0.020

enables us to take into account the difference in brightness between the analysed soil materials. These curves were obtained from the individual soil *NR* curves by multiplying their *NR* data by the ratio of a given soil radiance to the radiance of the standard panel, both collected at nadir at the same solar zenith angle. Reflectance curves generated in this way make it possible to predict in which illumination and viewing conditions the spectral contrast between analysed surfaces is highest. These curves show that viewing these surfaces from the nadir makes it relatively difficult to separate the sand from the playa and the crust from the reg. It is clearly easier to separate them when they are observed obliquely. The contrast between the sand and the playa becomes higher if the sensor looks from the backscattering directions at view zenith angles higher than 20° and at solar zenith angles between 35° and 65°. However the contrast between the crust and the reg rises if the sensor observes them from the forwardscattering directions, at zenith angles lower than −50° and especially at extremely high solar zenith angles (e.g. 80°).

The examples discussed here enable us to understand better the interaction of electromagnetic radiation with soil surfaces under different geometric conditions. These virtual surfaces can be used for re-constructing the bidirectional reflectance factors of soil surfaces from a limited sample of angular reflectance measurements and to convert remote sensing data collected under different illumination and viewing conditions to standardize forms, which will contribute to improved interpretations. The procedure described in this paper offers a major contribution for different types

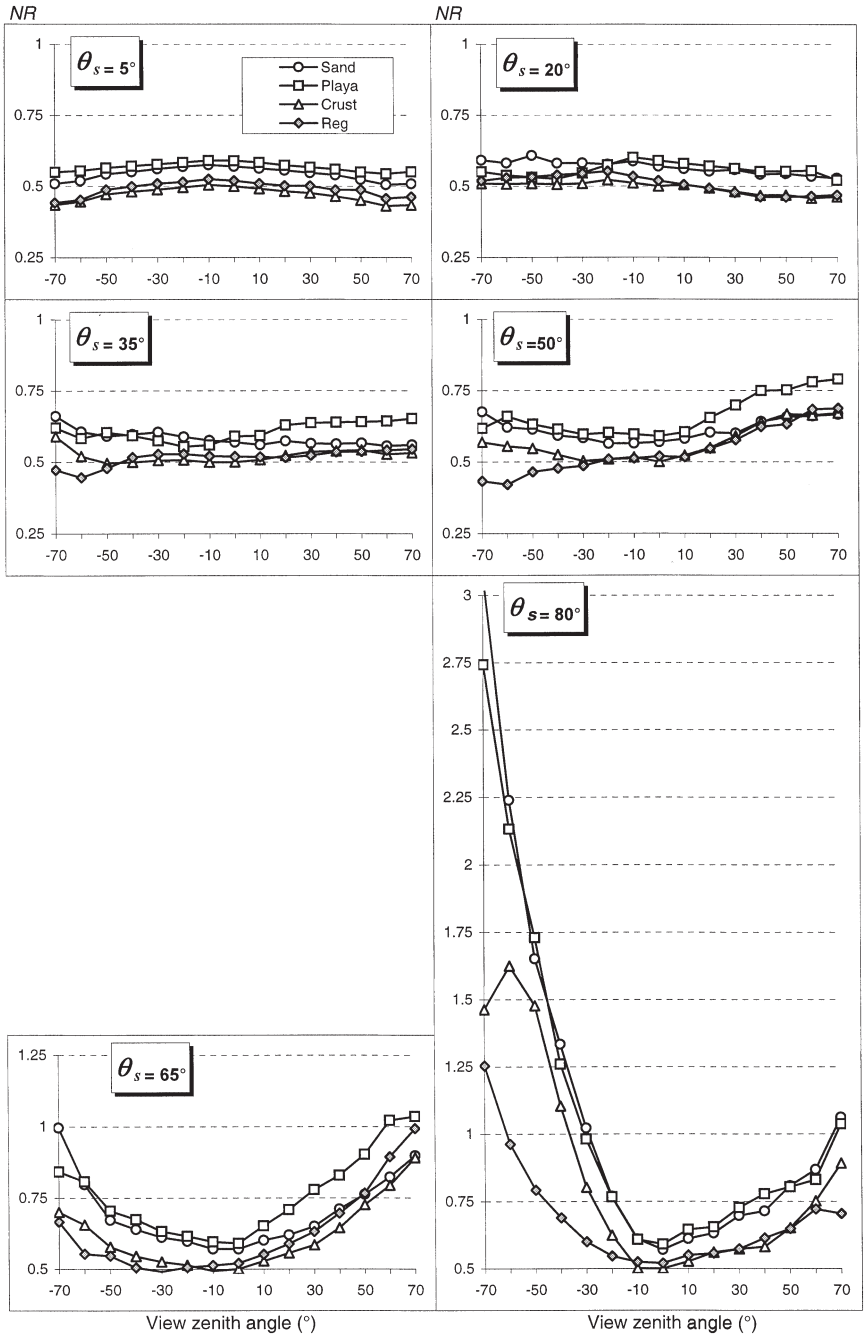

Figure 8. Reflectance curves for the analysed soil surfaces along the solar principal plane for the 850 nm channel predicted using their virtual surfaces for selected solar zenith angles θ_s.

of operational space systems: (1) wide field-of-view (FOV) sensors, such as NOAA-AVHRR or SPOT 4-VEGETATION; (2) narrow FOV sensors tilted at different angles such as SPOT-HRV; and (3) conical scanning sensors of the ERS-1 ATSR

type. The potential of reflectance data recorded at several sensor view angles will increase with the launching in the near future of new instruments of NASA's Earth Observing System: the Moderate Resolution Imaging Spectrometer (MODIS) having an along-track viewing capability of up to $\pm 55^\circ$, and the Multi-angle Imaging SpectroRadiometer (MISR) acquiring multiple images of the Earth's surface at different sensor view angles in the range $\pm 58^\circ$ within a single orbital overpass (Barnsley 1994). Those virtual surfaces can also be applied to accurate estimates of the albedo of soil surfaces, a parameter of great importance in climate modelling.

4. Conclusions

The model presented in this paper, using the virtual soil surfaces (being a set of input data describing the geometry and reflectance features of each soil), has enabled us to predict the directional reflectance behaviour of semiarid soil surfaces, namely regs, crusts, playas and sands, in any illumination and viewing conditions. The geometry of these virtual surfaces has been described with spheroids of given horizontal and vertical radii lying on a freely sloping plane. They are absorbed into the ground of the slope plane with their tops projecting at a given height above the ground. The spheroids are regularly arranged in a square grid pattern on the slope.

The virtual surface of the reg is essentially different from the other analysed surfaces in terms of the size of its irregularities and its shape. It is described by spheroids having vertical elongation 3.3–5 times higher than those representing the remaining surfaces, whose spheroids are almost spherical. The spheroids of the virtual surface simulating the crust, which clearly displays more roughness than the playa and the sand, are only slightly absorbed into the plane of the ground. The virtual playa's spheroids are flattened, while the spheroids of the sand's surface are a little vertically elongated. The spheroids of both surfaces are absorbed deeper into the ground and arranged with larger distances between them than the crust's spheroids.

The large proportion of flat spaces between the virtual spheroids and the relatively flat tops of the spheroids enabled us to generate with the model the soil NR curves along the solar principal plane having a low variation of NR with view zenith angle. Flat fragments of soil virtual surfaces were also useful for generating the specular effects of the soil reflectance characteristic of smooth surfaces like the sand and the playa. The virtual surface simulating the crust, with the vertically elongated spheroids slightly absorbed into the ground, shows essentially less obvious specular effects and a prominent variability of the NR in the backscattering directions. Similar NR curves were generated by the reg virtual surface, although their geometry is clearly different.

Acknowledgments

Special thanks to Dr Charles Ichoku (NASA GSFC, Greenbelt, MD 20771) for his critical review of the manuscript and helpful comments. We thank the Hebrew University of Jerusalem Minerva Arid Ecosystems Research Centre for letting us use the site for the spectral measurements.

References

Barnsley, M. J., 1994, Environmental monitoring using multiple-angle (MVA) remotely-sensed data. *Environmental Remote Sensing from Regional to Global Scales*. John Wiley & Sons, Chichester, New York, Brisbane, Toronto, Singapore, pp. 181–201.

Cierniewski, J., 1987, A model for soil surface roughness influence on the spectral response bare soils in the visible and near-infrared range. *Remote Sensing of Environment*, **23**, 97–115.

Cierniewski, J., 1989, The influence of the viewing geometry of bare rough soil surfaces on

their spectral response in the visible and near-infrared image. *Remote Sensing of Environment*, **27**, 135–142.

Cierniewski, J., 1999, *Geometrical modelling of soil bidirectional reflectance in the optical domain*. Bogucki Scientific Publishers, Poznan, p. 148.

Cierniewski, J., and Verbrugghe, M., 1994, A geometrical model of soil bidirectional reflectance in the visible and near-infrared range. *Proceedings of 6th International Symposium on Physical Measurements and Signatures in Remote Sensing, Val d'Is're France, 17–21 January, 1994*, edited by G. Guyot (CNES), pp. 635–642.

Cierniewski, J., and Verbrugghe, M., 1997, Influence of soil surface roughness on soil bidirectional reflectance. *International Journal of Remote Sensing*, **18**, 1277–1288.

Cierniewski, J., Baret, F., Verbrugghe, M., Hanocq, J., and Jacquemud, S., 1996, Geometrical modelling of soil bidirectional reflectance incorporating specular effects. *International Journal of Remote Sensing*, **17**, 3691–3704.

Cooper, K. D., and Smith, J. A., 1985, A Monte Carlo reflectance model for soil surfaces with three-dimensional structure. *IEEE Transactions on Geoscience and Remote Sensing*, **1GE-23**, 668–667.

Coulson, K. L., 1966, Effect of reflection properties on natural surfaces in aerial reconnaissance. *Applied Optics*, **5**, 905–917.

Coulson, K. L., and Reynolds, D. W., 1971, The spectral reflectance of natural surfaces. *Journal of Applied Meteorology*, **10**, 1285–1295.

Danin, A., 1991, Plant adaptation in desert dunes. *Journal of Arid Environment*, **21**, 193–212.

Danin, A., Bar-Or, Y., Dor, I., and Yisraeli, T., 1989, The role of cyanobacteria in the stabilization of sand dunes in southern Israel. *Ecologia Mediterranea*, **15**, 55–64.

Deering, D. W., Eck, T. F., and Otterman, J., 1990, Bidirectional reflectance of selected desert surfaces and their three-parameter soil characterization. *Agricultural and Forest Meteorology*, **52**, 71–90.

Eaton, F. D., and Dirmhirn, I., 1979, Reflected irradiance indicatrices of natural surfaces and their effect on albedo. *Applied Optics*, **18**, 994–1003.

Evenari, M., Shanan, L., and Tadmor, N., 1982, *The Negev. The Challenge of a Desert* (Cambridge: Harvard University Press).

Hapke, B., 1981, Bidirectional reflectance spectroscopy 1. Theory. *Journal of Geophysical Research*, **86**, 3039–3054.

Hapke, B., 1984, Bidirectional reflectance spectroscopy 3. Correction for macroscopic roughness. *Icarus*, **59**, 41–59.

Hapke, B., 1986, Bidirectional reflectance spectroscopy 4. The extinction coefficient and the opposition effect. *Icarus*, **67**, 264–280.

Irons, J. R., Campbell, G. S., Norman, J. M., Graham, D. W., and Kovalick, W. M., 1992, Prediction and measurement of soil bidirectional reflectance. *IEEE Transactions on Geoscience and Remote Sensing*, **30**, 249–260.

Jacquemoud, S., Baret, F., and Hanocq, J. F., 1992, Modelling spectral and bidirectional soil reflectance. *Remote Sensing of Environment*, **41**, 123–132.

Karnieli, A., 1997, Development and implementation of spectral crust index over dune sands. *International Journal of Remote Sensing*, **18**, 1207–1220.

Karnieli, A., and Tsoar, H., 1995, Satellite spectral reflectance of biogenic crust developed in desert dune sand along the Israel-Egypt border. *International Journal of Remote Sensing*, **16**, 369–374.

Norman, J. M., Welles, J. M., and Walter, E. A., 1985, Contrast among bidirectional reflectance of leaves, canopies, and soils. *IEEE Transactions on Geoscience and Remote Sensing*, **23**, 659–667.

Otterman, J., 1981, Reflection from soil with sparse vegetation. *Advances in Space Research*, **1**, 115–119.

Otterman, J., and Tucker, C. J., 1985, Satellite measurements of surface albedo and temperatures in semi desert. *Journal of Climate Applied Meteorology*, **24**, 228–233.

Pinty, B., Verstraete, M. M., and Dickinson, R. E., 1989, A physical model for predicting bidirectional reflectance over bare soil. *Remote Sensing of Environment*, **27**, 273–288.

Shoshany, M., 1993, Roughness-reflectance relationship of bare desert terrain, an empirical study. *Remote Sensing of Environment*, **45**, 15–27.

Walthall, C. L., Norman, J. M., Walles, J. M., Campbell, G., and Blad, B. L., 1985, A simple equation to approximate the bidirectional reflectance from vegetative canopies and bare soil surfaces. *Applied Optics*, **24**, 383–387.